Magnetoresistance of normal conductor/insulator/perfect conductor composites with a columnar microstructure

David J. Bergman[1,2] and Yakov M. Strelniker[1,*]
[1]*School of Physics and Astronomy, Raymond and Beverly Sackler Faculty of Exact Sciences, Tel Aviv University, Tel Aviv 69978, Israel*
[2]*Department of Physics, The Ohio State University, Columbus, Ohio 43210-1106*
(Received 21 January 2000; revised manuscript received 3 August 2000)

The in-plane magnetoresistance of columnar composites is studied for a class of three-constituent mixtures of normal conductor, perfect insulator, and perfect conductor, where the magnetic field **B** is applied in the plane perpendicular to the columnar axis. Exact relations are found between the bulk effective resistivity tensor $\hat{\rho}_e$ of such a medium and that of a medium where the perfect insulator and perfect conductor have exchanged their spatial locations. Exact expressions are found in some cases for the leading order large **B** behavior of $\hat{\rho}_e$, for periodic microstructures and certain directions and ranges of directions of **B**. Numerical calculations are used to compute $\hat{\rho}_e$ in those microstructures for all directions of **B**, and for various magnitudes of $|\mathbf{B}|$. The different results are compared and their significance is discussed.

I. INTRODUCTION

The magnetotransport properties of composite media have been subject to increased attention in recent years. Some of this involves microstructures where one of the constituents is ferromagnetic, leading to the phenomenon of ''giant magnetoresistance.''[1,2] However, even when none of the constituents have any unusual magnetic properties, other than the normal classical Hall effect which is present in all electronic conductors, some surprising phenomena are found to appear. Those include a bulk effective magnetoresistivity which oscillates rapidly with changing directions of the magnetic field **B** and the average current density $\langle \mathbf{J} \rangle$, when **B** is large enough, in the case of a periodic microstructure, even if that microstructure has a very high point symmetry, such as cubic or square.[3,4] The most striking effects were predicted for two-constituent columnar microstructures that are periodic in the plane perpendicular to the columnar axis, where a periodic array of inclusions is embedded in a normal conducting host, denoted by *M*, and the inclusions are either perfectly insulating, denoted by *I*, or perfectly conducting, denoted by *S*. Those effects appear when **B** lies in that plane and is strong enough so that the Hall-to-Ohmic resistivity ratio of the *M* constituent $H \equiv \rho_{\mathrm{Hall}}/\rho_{\mathrm{Ohmic}} = \mu|\mathbf{B}|$ (μ is the Hall mobility of that constituent) satisfies $|H| > 1$. In that case, not only do the in-plane components of the bulk effective resistivity tensor $\hat{\rho}_e$ oscillate strongly when **B** is rotated in that plane, but they also often exhibit a nonsaturating behavior, forever increasing as H^2 when $|H| \gg 1$.[5,6]

Another surprising result of those studies was that, quite often, the local current distribution in such periodic microstructures becomes very simple in the limit $|H| \gg 1$. Thus, when the inclusion shapes and their periodic arrangement are very simple, (e.g., square array of parallel circular cylinders or square cross-section rods), the asymptotic current distribution $\mathbf{J}(\mathbf{r})$ can be calculated in closed form if **B** lies along a low order lattice axis of the array. Consequently, closed form expressions were also derived for the bulk effective longitudinal resistivity $\rho_{\|}^{(e)}$ and the bulk effective in-plane transverse resistivity $\tilde{\rho}_{\perp}^{(e)}$.[5,6] In another recent study, an extension of the classical duality transformation of two-dimensional (2D) conductors was used to derive exact relations between the resistivity components of an M/I columnar composite mixture and those of an M/S mixture with the *same microstructure*.[7] Recently, a study of disordered, two-constituent columnar composites of M/I and M/S mixtures, using a modification of the Bruggeman self-consistent effective-medium approximation, showed that such systems also exhibit interesting behavior when $|H| \gg 1$.[8] Very recently, a similar study of a disordered, *three-constituent* $M/I/S$ columnar composite revealed that such systems exhibit a critical point which is due to a different type of percolation process.[9]

In this paper, we report on other studies of *three-constituent* columnar composite media, where both *I* and *S* inclusions are embedded in an *M* host. In particular, we focus our attention on such mixtures where the 2D microstructure is *periodic*. Such three-constituent $M/I/S$ microstructures, while they are more difficult to fabricate than periodic two-constituent M/I or M/S microstructures, are expected to allow greater flexibility in manipulating the macroscopic response.

We first show that the three-dimensional (3D) transport problem in such a medium can be reduced to a 2D problem in the plane perpendicular to the columnar axis. We then use the classical duality transformation for such a medium to obtain some exact relations between the bulk effective resistivity tensor $\hat{\rho}_e$ of a columnar $M/I/S$ mixture and that of the ''I/S exchanged composite,'' denoted by $\hat{\rho}_{ex}$, where the *I* and *S* constituents have exchanged their spatial locations. All this is done in Sec. II.

In Sec. III we develop some general principles for conducting an asymptotic analysis of the strong field (i.e., $|H| \gg 1$) behavior of periodic, three-constituent, $M/I/S$ columnar microstructures. We derive expressions for the leading-order large *H* behavior of the bulk effective resistivity components $\rho_{\|}^{(e)}$ and $\tilde{\rho}_{\perp}^{(e)}$ in some such microstructures. This is done by first finding the asymptotic local electric current and

field distributions using considerations and methods that were developed earlier.[6,10] This can usually be done only if **B** lies in some selected directions, or in some restricted ranges of directions. In those ranges, it is found that the macroscopic response of the system can sometimes be reproduced by a simple regular resistor network, with resistances that can be calculated from the asymptotic analysis. This greatly simplifies the analysis of such systems. The results for $\rho_{\|}^{(e)}$ and $\tilde{\rho}_{\perp}^{(e)}$ are tested on some of the exact relations derived in Sec. II.

In Sec. IV we use a numerical procedure, developed earlier for calculating $\hat{\rho}_e$ of periodic microstructures,[11] in order to compute $\hat{\rho}_e$ for all in-plane directions of **B**, and for various finite values of H. Those results are exhibited as polar plots of the different components of $\hat{\rho}_e$, and are compared both with the exact relations of Sec. II, and with the asymptotic expressions found in Sec. III.

Section V includes a discussion of our main results, as well as suggestions for further directions of research in this area.

II. THEORY

We will always choose the x coordinate to lie along the columnar axis. The local conductivity tensor $\hat{\sigma}(\mathbf{r})$ will thus be independent of x. The local electric field $\mathbf{E}(\mathbf{r})$ and current density or flux $\mathbf{J}(\mathbf{r})$ will also be independent of x, but will usually have nonzero components along x, y, and z, especially when an external magnetic field **B** is applied. From the fact that $\nabla\times\mathbf{E}=0$ it then follows that the columnar component of **E**, namely E_x, is constant everywhere.[12] Because **J** is independent of x, the three-dimensional (3D) equation $\nabla\cdot\mathbf{J}=0$ only involves J_y and J_z, the components of **J** in the y,z plane that is perpendicular to the columnar axis x. If the boundary conditions dictate that $E_x=0$, then the electrical potential $\phi(\mathbf{r})$ is also independent of x, and the equation $\nabla\cdot\hat{\sigma}(\mathbf{r})\cdot\nabla\phi(\mathbf{r})=0$ reduces to a two-dimensional (2D) equation in the y,z plane.

It is then possible to define a dual 2D conductivity problem, by rotating the y and z components of **E** and **J** by 90° in the y,z plane at every point in that plane, and calling the rotated fields $\mathbf{J}_D$ and $\mathbf{E}_D$, respectively.[13] These are the dual current density or flux and dual electric field, and they satisfy the 2D equations $\nabla\times\mathbf{E}_D=\nabla\cdot\mathbf{J}_D=0$ in the y,z plane. From the relation

$$\mathbf{J}(\mathbf{r})=\hat{\sigma}(\mathbf{r})\cdot\mathbf{E}(\mathbf{r}),\quad \hat{\sigma}\equiv\begin{pmatrix}\sigma_{yy} & \sigma_{yz}\\ \sigma_{zy} & \sigma_{zz}\end{pmatrix}, \tag{2.1}$$

which exists between the original 2D in-plane components of **E** and **J**, it follows that the dual fields are related by[14]

$$\mathbf{J}_D(\mathbf{r})=\hat{\sigma}_D(\mathbf{r})\cdot\mathbf{E}_D(\mathbf{r}),\quad \frac{1}{\hat{\sigma}_D}\equiv\begin{pmatrix}\sigma_{zz} & -\sigma_{zy}\\ -\sigma_{yz} & \sigma_{yy}\end{pmatrix}, \tag{2.2}$$

$$\hat{\sigma}_D=\frac{1}{\det\hat{\sigma}}\begin{pmatrix}\sigma_{yy} & \sigma_{zy}\\ \sigma_{yz} & \sigma_{zz}\end{pmatrix}. \tag{2.3}$$

We note that if $\sigma_{yz}=\sigma_{zy}$, then $\hat{\sigma}_D=\hat{\sigma}/\det\hat{\sigma}$, and that if $\sigma_{yz}=\sigma_{zy}=0$, then $\sigma_{Dyy}=1/\sigma_{zz}$ and $\sigma_{Dzz}=1/\sigma_{yy}$.

We are interested in the case where, in one of the constituents, $\hat{\sigma}(\mathbf{r})$ represents an isotropic conductor M, with an in-plane external magnetic field **B**. Choosing the z coordinate axis to lie along **B**, the 3D conductivity and resistivity tensors, $\hat{\sigma}_M$ and $\hat{\rho}_M=1/\hat{\sigma}_M$, have the forms

$$\hat{\rho}_M=\rho_0\begin{pmatrix}1 & -H & 0\\ H & 1 & 0\\ 0 & 0 & \nu\end{pmatrix}, \tag{2.4}$$

$$\hat{\sigma}_M=\frac{1}{\rho_0}\begin{pmatrix}\frac{1}{1+H^2} & \frac{H}{1+H^2} & 0\\ \frac{-H}{1+H^2} & \frac{1}{1+H^2} & 0\\ 0 & 0 & \frac{1}{\nu}\end{pmatrix}, \tag{2.5}$$

where $H=\mu|\mathbf{B}|$ is the Hall-to-transverse-Ohmic resistivity ratio in the M constituent and μ is its Hall mobility. The 2D in-plane part of $\hat{\sigma}_M$ is simpler than the full 3D tensor because it is diagonal. Moreover, the 2D dual conductivity tensor $\hat{\sigma}_{DM}$ is proportional to the 2D part of $\hat{\sigma}_M$ (where no confusion can arise, we will use the same symbol to denote a full 3D tensor as well as its 2×2 lower right block of y,z components):

$$\hat{\sigma}_M=\frac{1}{\rho_0}\begin{pmatrix}\frac{1}{1+H^2} & 0\\ 0 & \frac{1}{\nu}\end{pmatrix}, \tag{2.6}$$

$$\hat{\sigma}_{DM}=\rho_0\begin{pmatrix}\nu & 0\\ 0 & 1+H^2\end{pmatrix}=\rho_0^2\nu(1+H^2)\hat{\sigma}_M. \tag{2.7}$$

The other constituents are a perfect insulator, denoted by I and characterized in the y,z plane by

$$\hat{\sigma}_I=\begin{pmatrix}0 & 0\\ 0 & 0\end{pmatrix},\quad \hat{\sigma}_{DI}=\begin{pmatrix}\infty & 0\\ 0 & \infty\end{pmatrix}, \tag{2.8}$$

and a perfect conductor, denoted by S and similarly characterized by

$$\hat{\sigma}_S=\begin{pmatrix}\infty & 0\\ 0 & \infty\end{pmatrix}=\hat{\sigma}_{D\,I},\quad \hat{\sigma}_{D\,S}=\begin{pmatrix}0 & 0\\ 0 & 0\end{pmatrix}=\hat{\sigma}_I. \tag{2.9}$$

Solutions of the original 3D conductivity problem can be used to determine the macroscopic or bulk effective 3D conductivity and resistivity tensors, $\hat{\sigma}_e$, $\hat{\rho}_e=1/\hat{\sigma}_e$. These tensors characterize the linear relation between the volume averaged value of the current density $\langle\mathbf{J}\rangle$ and that of the electric field $\langle\mathbf{E}\rangle$

$$\langle\mathbf{J}\rangle=\hat{\sigma}_e\cdot\langle\mathbf{E}\rangle. \tag{2.10}$$

In a columnar system, the constancy of E_x leads to a number of exact relations among the various elements of $\hat{\rho}_e$.[8] In the case where one of the constituents is a perfect conductor, the fact that $E_x \equiv 0$, whatever the value of $\langle \mathbf{J} \rangle$, leads to the simple results[8,7]

$$\rho_{xx}^{(e)} = \rho_{xy}^{(e)} = \rho_{yx}^{(e)} = \rho_{xz}^{(e)} = \rho_{zx}^{(e)} = 0. \tag{2.11}$$

Thus, only the 2D tensor, consisting of the 2×2 block in the lower right corner of $\hat{\rho}_e$, is nonzero. That 2D resistivity tensor is just the inverse of the y,z plane 2D part of $\hat{\sigma}_e$, which can be obtained by solving a 2D conductivity problem in the y,z plane, where $\hat{\sigma}(\mathbf{r})$ is a 2D diagonal tensor even in the presence of an in-plane magnetic field. The resulting 2D tensor $\hat{\sigma}_e$, while in general nondiagonal, will always be symmetric. For a given microstructure, $\hat{\sigma}_e$ can be viewed as a function of the constituent conductivity tensors $\hat{\sigma}_i$ which is homogeneous of order 1, namely

$$\hat{\sigma}_e(\lambda \hat{\sigma}_1, \lambda \hat{\sigma}_2, \ldots) = \lambda \hat{\sigma}_e(\hat{\sigma}_1, \hat{\sigma}_2, \ldots). \tag{2.12}$$

The bulk effective conductivity tensor of the dual problem $\hat{\sigma}_{D\,e}$ is obtained by a similar procedure, where the various constituents are characterized by their dual conductivity tensors $\hat{\sigma}_{D\,i}$, but are put together with the *same microstructure* as the original problem which lead to the function $\hat{\sigma}_e(\hat{\sigma}_1, \hat{\sigma}_2, \ldots)$. Therefore the dependence of $\hat{\sigma}_{D\,e}$ upon $\hat{\sigma}_{D\,i}$ is given by that *same function*

$$\hat{\sigma}_{D\,e} = \hat{\sigma}_e(\hat{\sigma}_{D\,1}, \hat{\sigma}_{D\,2}, \ldots). \tag{2.13}$$

Applying Eqs. (2.7), (2.9), (2.12), and (2.13) to the case of a three constituent $M/I/S$ mixture, we get

$$\begin{aligned} \hat{\sigma}_{De} &= \hat{\sigma}_e(\hat{\sigma}_{D\,M}, \hat{\sigma}_{D\,I}, \hat{\sigma}_{D\,S}) \\ &= \hat{\sigma}_e[\rho_0^2 \nu(1+H^2)\hat{\sigma}_M, \hat{\sigma}_S, \hat{\sigma}_I] \\ &= \rho_0^2 \nu(1+H^2)\hat{\sigma}_e(\hat{\sigma}_M, \hat{\sigma}_S, \hat{\sigma}_I). \end{aligned} \tag{2.14}$$

From Eq. (2.3), noting that $\sigma_{yz}^{(e)} = \sigma_{zy}^{(e)}$, we then conclude that the bulk effective 2D (y,z plane) conductivity tensor $\hat{\sigma}_e \equiv \hat{\sigma}_e(\hat{\sigma}_M, \hat{\sigma}_I, \hat{\sigma}_S)$ of any columnar $M/I/S$ mixture is proportional to the bulk effective 2D conductivity tensor of the ''I/S constituent exchanged composite'' $\hat{\sigma}_{ex} \equiv \hat{\sigma}_e(\hat{\sigma}_M, \hat{\sigma}_S, \hat{\sigma}_I)$, where the I and S constituents have exchanged their spatial locations

$$\hat{\sigma}_{ex} = \frac{1}{\rho_0^2 \nu(1+H^2)} \frac{\hat{\sigma}_e}{\det \hat{\sigma}_e}. \tag{2.15}$$

This can also be written in terms of the 2D (y,z plane) resistivity tensors $\hat{\rho}_e$ and $\hat{\rho}_{ex}$ of the I/S constituent exchanged columnar composites

$$\hat{\rho}_{ex} = \hat{\rho}_e \frac{\rho_0^2 \nu(1+H^2)}{\det \hat{\rho}_e}. \tag{2.16}$$

A special case occurs when the microstructure is symmetric, i.e., it is at least macroscopically invariant under the above described spatial exchange of the I and S constituents $\hat{\rho}_{ex} = \hat{\rho}_e$. In that case, these exact relations reduce to the following relation between the three nonzero in-plane components of $\hat{\rho}_e$, namely, $\rho_{\parallel}^{(e)} \equiv \rho_{zz}^{(e)}$, $\tilde{\rho}_{\perp}^{(e)} \equiv \rho_{yy}^{(e)}$, and the off-diagonal component $\rho_{yz}^{(e)}$:

$$\det \hat{\rho}_e \equiv \rho_{\parallel}^{(e)} \tilde{\rho}_{\perp}^{(e)} - (\rho_{yz}^{(e)})^2 = \rho_0^2 \nu(1+H^2). \tag{2.17}$$

The last relation can also be expressed in terms of the corresponding components of $\hat{\sigma}_e$:

$$\det \hat{\sigma}_e \equiv \sigma_{\parallel}^{(e)} \tilde{\sigma}_{\perp}^{(e)} - (\sigma_{yz}^{(e)})^2 = \frac{1}{\rho_0^2 \nu(1+H^2)}. \tag{2.18}$$

These relations are highly nontrivial: In the case of a columnar microstructure which has a 2D periodicity and a strong in-plane **B** field, the resistivities $\rho_{\parallel}^{(e)}$, $\tilde{\rho}_{\perp}^{(e)}$, $\rho_{yz}^{(e)}$, as well as the I/S constituent exchanged resistivities $\rho_{\parallel}^{(ex)}$, $\tilde{\rho}_{\perp}^{(ex)}$, $\rho_{yz}^{(ex)}$, will exhibit strong fluctuations as **B** is rotated in that plane. Thus the fact that $\hat{\rho}_{ex} \propto \hat{\rho}_e$ in Eq. (2.16), and the fact that the combination of elements of $\hat{\rho}_e$ which appears in Eq. (2.17) has a constant value independent of the direction of **B**, are very strong statements. From Eqs. (2.15) or (2.16) it also follows that

$$\frac{\rho_{\parallel}^{(e)}}{\tilde{\sigma}_{\perp}^{(e)}} = \frac{\tilde{\rho}_{\perp}^{(e)}}{\sigma_{\parallel}^{(e)}} = -\frac{\rho_{yz}^{(e)}}{\sigma_{yz}^{(e)}} = \rho_0^2 \nu(1+H^2) \tag{2.19}$$

for a symmetric microstructure.

When the composite is not I/S-constituent-exchange symmetric, some exact relations can be written between elements of $\hat{\rho}_e$ and those of $\hat{\rho}_{ex}$. Those relations, which follow from Eq. (2.16) [see also Eqs. (4.6)–(4.7) in Ref. 7, which express somewhat similar relations for a *two-constituent* composite], are

$$\frac{\rho_{yz}^{(e)}}{\rho_{yz}^{(ex)}} = \frac{\rho_{\parallel}^{(e)}}{\rho_{\parallel}^{(ex)}} = \frac{\tilde{\rho}_{\perp}^{(e)}}{\tilde{\rho}_{\perp}^{(ex)}} = \frac{\det \hat{\rho}_e}{\rho_0^2 \nu(1+H^2)} = \frac{\rho_0^2 \nu(1+H^2)}{\det \hat{\rho}_{ex}}. \tag{2.20}$$

Obviously, multiplication of any of these quotients by either $\det \hat{\rho}_{ex}$ or $1/\det \hat{\rho}_e$ would transform it into a quantity that is independent of the direction of **B**.

If we choose y,z to lie along the common principal axes of $\hat{\rho}_e$, $\hat{\rho}_{ex}$, then Eq. (2.16) reduces to

$$\rho_{yy}^{(ex)} \rho_{zz}^{(e)} = \rho_{zz}^{(ex)} \rho_{yy}^{(e)} = \rho_0^2 \nu(1+H^2). \tag{2.21}$$

The results of the modified effective medium approximation, for the asymptotic large H behavior of $\hat{\rho}_e$ in a disordered columnar $M/I/S$ mixture, satisfy this relation—see Eqs. (10) and (11) in Ref. 9. If $\nu = 1$ and $H = 0$, and if the microstructure is either isotropic in the y,z plane, or square or triangular or hexagonal there, then this equation further reduces to

$$\rho_{ex} \rho_e = \rho_0^2. \tag{2.22}$$

If the microstructure is also symmetric, then $\rho_e = \rho_{ex} = \rho_0$ irrespective of any further details of the microstructure.

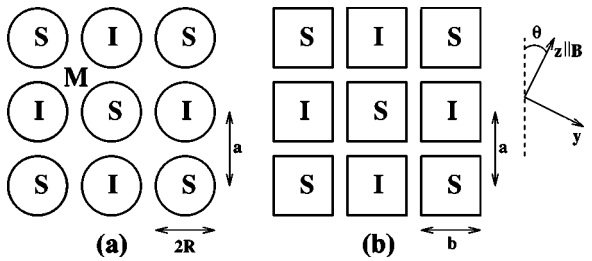

FIG. 1. Two types of symmetric, periodic, $M/I/S$ columnar composites considered in this article. The x axis is always taken to be the columnar axis, and is perpendicular to the plane of this figure. A magnetic field **B** is applied in that plane, and the z axis is always taken to lie along **B**. θ is the angle between **B** and the nearest principal axis of the square array.

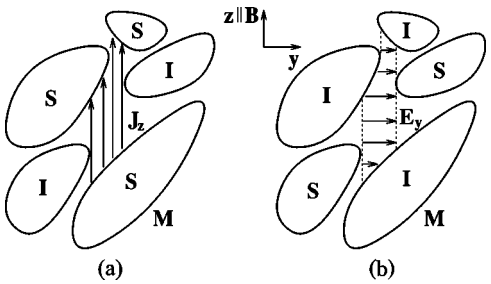

FIG. 2. Two basic types of configurations where the electrical transport between two S inclusions becomes very simple in the limit $|H|\gg 1$: In (a) there are **B**-parallel layers of M material which *connect* different S inclusions and are free of any I material. In that case, a potential difference between the S inclusions induces current flow *mainly along z*, with $J_z(y)$ that is *independent of z* and inversely proportional to the distance along z, $l_z(y)$, between adjacent edges of those inclusions. In (b) there are **B**-parallel layers of M material which *separate* between different S inclusions and are free of any I material. In that case, a potential difference between the S inclusions induces an electric field *mainly along y*, with $E_y(y)$ that is *independent of z* and inversely proportional to $l_z(y)$, which now represents the length of those **B**-parallel layers, and is equal to the distance along z between adjacent edges of the I inclusions that determine the ends of those layers. The particular configurations shown in (a) and (b) are related to each other by the classical duality transformation.

III. EXACT ASYMPTOTIC RESULTS FOR PERIODIC MICROSTRUCTURES AT LARGE B

A. General considerations

We consider a columnar microstructure composed of an isotropic conductor host, denoted by M, inside of which is embedded a periodic square array of infinitely long parallel inclusions of constant cross section. The electrical properties of those inclusions alternate between perfectly insulating, denoted by I, and perfectly conducting, denoted by S. Two particularly simple microstructures of this kind, both of which are also symmetric or invariant under the exchange of the I and S constituents, are shown in Fig. 1. A magnetic field $\mathbf{B}\|z$ is always applied in the plane perpendicular to the columnar axis x.

We now establish some general principles that govern the asymptotic electrical response of such microstructures when $|H|\gg 1$. For this it is of crucial importance that $\sigma_{zz}^{(M)} \gg \sigma_{yy}^{(M)}$, and that each S inclusion represents an equipotential. For those reasons, if a parallel layer of M material along z can be found which connects between a pair of S inclusions that are at different potentials, then current will flow between those inclusions only through that layer and only along z, to leading order in powers of $1/H$—see Fig. 2(a). Such a flow pattern minimizes the dissipation due to a given potential difference $\Delta\phi$ between those inclusions. Because $J_y \ll J_z$ in that layer [by a factor of order H^2—see Eq. (2.6)], therefore J_z must be constant along each flow line $J_z = J_z(y)$. Consequently, $E_z(y)$ will also be constant along each flow line, and its value will be given by

$$E_z(y) = \frac{\Delta\phi}{l_z(y)}, \tag{3.1}$$

where $l_z(y)$ is the y-dependent separation, along z, between adjacent edges of the two S inclusions. Note, however, that although $J_y \ll J_z$, E_y will, in general, have a magnitude similar to that of E_z. In spite of this, the contribution of E_y to the dissipation will be smaller than that of E_z by a factor of order H^2.

A case where no such **B**-parallel layer of M material *connects* between a pair of S inclusions that are at different potentials is shown in Fig. 2(b), where a configuration is depicted which is just the dual of the one shown in Fig. 2(a). In that case one can always find **B**-parallel layers which *separate* the two S inclusions, as is the case in Fig. 2(b). In those regions $E_z \ll E_y$ by a factor of order H^2—this is just the dual of the situation encountered in the previous problem. This can also be deduced by minimizing the total dissipation resulting from a given potential difference between the two S inclusions. From the duality connection between Figs. 2(a) and 2(b) we also conclude that E_y is independent of z, $E_y = E_y(y)$, therefore $J_y = J_y(y)$ is also independent of z. This can also be deduced from the requirement that $\nabla\times\mathbf{E}=0$. Again, although J_z will be of the same order of magnitude as J_y, its contribution to the total dissipation is smaller than that of J_y by a factor of order H^2. [This is so because the inverse of the 2D conductivity tensor of Eq. (2.6) has a yy component that is greater than its zz component by such a factor.] From the above-mentioned duality connection we also deduce that $E_y(y) \propto 1/l_z(y)$, where $l_z(y)$ is now the distance, through M and along z, between two neighboring I inclusions that define the ends of the **B**-parallel separating layers—see Fig. 2(b). We can also deduce this from the requirement that the product $J_y(y) l_z(y)$ must be independent of y in those layers. The coefficient of proportionality can be found from the requirement

$$\Delta\phi = \int dy E_y(y), \tag{3.2}$$

where $\Delta\phi$ is the potential difference between the two S inclusions, and the limits of integration are the extreme values of y determined by the S inclusions—see Fig. 2(b).

B. Application to the case where B points in a general direction

We now apply the principles of Sec. III A to the case of Figs. 1(a) and 1(b), when **B** points in a somewhat general direction, subtending an angle θ with one of the principal

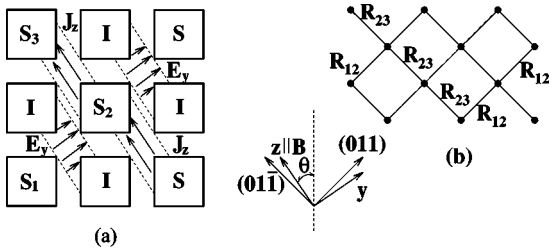

FIG. 3. (a) Symmetric, square array of alternating I and S rods, embedded in a host M, with $\mathbf{B}$ along a general, nonsymmetry direction, making an angle θ with the nearest principal axis. If the inclusions are large enough and θ is not too small, then the transport between S_2 and S_3 is a special case of the configuration shown in Fig. 2(a), while the transport between S_1 and S_2 is a special case of the configuration shown in Fig. 2(b). (b) Resistor network whose macroscopic response reproduces that of the actual composite shown in (a) when $|H|\gg 1$. The principal axes of the network are the (011) and $(01\bar{1})$ lattice axes of the actual composite structure. The resistors are R_{12} along (011) and R_{23} along $(01\bar{1})$. The values of R_{12} and R_{23} are given by Eqs. (3.7) and (3.3) for square-rod-shaped inclusions, and by Eqs. (3.8) and (3.4) for circular-cylinder-shaped inclusions.

axes of the periodic array. This angle will be somewhat restricted as indicated below. For simplicity, we restrict our discussion to the case of inclusions which are large enough, and angles θ which are also large enough, so that the situations depicted in Figs. 2(a) and 2(b) always occur, but only between nearest-neighbor S inclusions. Focusing upon the inclusions marked as S_1, S_2, S_3 in Fig. 3(a), it is clear that S_2, S_3 are in the situation of Fig. 2(a), while S_1, S_2 are in the situation of Fig. 2(b). Assuming a given potential difference between S_2, S_3, it is a straightforward matter to calculate the total current flowing between those inclusions in the limit $|H|\gg 1$. We can then define an effective resistance R_{23} as the ratio between that potential difference and the total current. This comes out as (note that we are taking ρ_0 to be a 2D resistivity, thus it has the same physical dimensions as the resistance R_{23})

$$R_{23}=\frac{2\nu\rho_0}{\sin 2\theta[1+2\ln(1+\tan\theta)]-2\sin^2\theta}$$

$$\text{for}\quad \arctan\left(\frac{a-b}{b}\right)\leqslant\theta\leqslant\frac{\pi}{4} \tag{3.3}$$

in the case of square-rod shaped inclusions of cross section $b\times b$ and nearest-neighbor center distance a, and will be used to characterize the electrical transport between S_2, S_3 for $|H|\gg 1$. A similar calculation, for the case of circular-cylinder-shaped inclusions of radius R and nearest-neighbor center distance a, as shown in Fig. 1(a), leads to

$$R_{23}=\frac{\nu\rho_0}{2F\left(\frac{R}{a},\theta\right)}\ \text{for}\ \frac{1}{\sqrt{2}}\leqslant\cos\theta\leqslant\frac{2R}{a}, \tag{3.4}$$

where

$$F(Z,\theta)=\int_0^{v_0}dv\left\{2\frac{\cos\theta+\sin\theta}{\cos\theta-\sin\theta}-\left[\left(\frac{2Z}{\cos\theta-\sin\theta}\right)^2-(1+v)^2\right]^{1/2}-\left[\left(\frac{2Z}{\cos\theta-\sin\theta}\right)^2-(1-v)^2\right]^{1/2}\right\}^{-1} \tag{3.5}$$

and

$$v_0\equiv\begin{cases}\dfrac{\cos\theta+\sin\theta-2Z}{\cos\theta-\sin\theta} & \text{for}\ \cos\theta\leqslant\dfrac{1}{2Z},\\[2ex] \dfrac{(1-\sqrt{4Z^2-1})\sin\theta}{\cos\theta-\sin\theta} & \text{for}\ \cos\theta\geqslant\dfrac{1}{2Z}.\end{cases} \tag{3.6}$$

The second line in the definition of v_0 is relevant only when $2Z\equiv 2R/a>1$, i.e., when there is partial overlap between nearest-neighbor cylinders.

Calculation of the current flowing between S_1, S_2 when $|H|\gg 1$, [see Fig. 3(a)] given a fixed potential difference between them, yields the effective resistance

$$R_{12}=\frac{1}{2}\rho_0H^2\{\sin 2\theta[1+2\ln(1+\tan\theta)]-2\sin^2\theta\}$$

$$=\frac{\nu\rho_0^2H^2}{R_{23}}\ \text{for}\ \arctan\left(\frac{a-b}{b}\right)\leqslant\theta\leqslant\frac{\pi}{4} \tag{3.7}$$

in the case of square-rod-shaped inclusions. A similar calculation for the case of circular-cylinder-shaped inclusions leads to

$$R_{12}=2\rho_0H^2F\left(\frac{R}{a},\theta\right)=\frac{\nu\rho_0^2H^2}{R_{23}}\ \text{for}\ \frac{1}{\sqrt{2}}\leqslant\cos\theta\leqslant\frac{2R}{a}. \tag{3.8}$$

The inequalities which θ must obey for these results to be valid can only be satisfied if $b/a\geqslant 1/2$ in the case of the rods, or if $R/a\geqslant 1/\sqrt{8}$ in the case of the cylinders. We note that, in the latter case, it is possible that neighboring cylinders overlap, and that the above expressions continue to be valid as long as there is no overlap between next-nearest neighbor cylinders, i.e., as long as $R<a/\sqrt{2}$. Under those overlap conditions for the circular cylinders, Eqs. (3.4) and (3.8) hold for $\mathbf{B}$ in *any in-plane direction*, with the exception of $\theta=0$, i.e., $\mathbf{B}\|(001)$—see Sec. III E below.

If the lower inequalities in Eqs. (3.3)–(3.8) are not satisfied, so that the angle θ between $\mathbf{B}$ and the closest principal axis of the inclusion array is less than $\arctan(a/b-1)$ or $\arccos(2R/a)$, then the equivalent resistor network becomes more complicated, i.e., it will have resistors connecting further than nearest-neighbor sites. We note the somewhat surprising fact that, for the square-shaped rods, though not for the circular cylinders, both R_{12} and R_{23} are independent of the inclusion sizes b within the restrictions described above. As we shall see in Secs. III C and III D below, this independence does not continue to hold in other configurations of the square-rods array.

For the purpose of evaluating asymptotic macroscopic response, we may now replace the actual continuum composite by a square network of resistors, where the sites or connec-

tion points represent the S inclusions and the resistors along one direction are all equal to R_{23}, while those in the perpendicular direction are all equal to R_{12}—see Fig. 3(b). Note that the principal axes of the resistor network are fixed along the (011) and $(01\overline{1})$ directions of the original square array of inclusions, but that the values of R_{12}, R_{23} depend on the magnitude as well as on the direction of **B**.

When this network model is valid, we can conclude that $\hat{\rho}_e$ has its principal axes along the fixed directions (011) and $(01\overline{1})$, and that the two principal 2D resistivities are just R_{12} and R_{23}. Using those, we can easily calculate asymptotic values of the more usual 2D components of $\hat{\rho}_e$, namely $\rho_{\parallel}^{(e)}$, $\tilde{\rho}_{\perp}^{(e)}$, $\rho_{yz}^{(e)}$

$$\rho_{\parallel}^{(e)} \cong \frac{1}{2}(1+\sin 2\theta)R_{23}+\frac{1}{2}(1-\sin 2\theta)R_{12}, \tag{3.9}$$

$$\tilde{\rho}_{\perp}^{(e)} \cong \frac{1}{2}(1-\sin 2\theta)R_{23}+\frac{1}{2}(1+\sin 2\theta)R_{12}, \tag{3.10}$$

$$\rho_{yz}^{(e)}=\rho_{zy}^{(e)} \cong \pm\frac{1}{2}\cos 2\theta(R_{12}-R_{23}), \tag{3.11}$$

where the $\pm$ signs in the last equation have to do with whether the direction of **B** is obtained by a clockwise or a counterclockwise rotation, by the angle θ, from the nearest principal axis: The lower sign ''$-$'' holds when that rotation is clockwise, the upper sign ''$+$'' holds when it is counterclockwise. Note that all the components of $\hat{\rho}_e$ increase as H^2 for $|H| \gg 1$, without any saturation, and that they also depend upon θ, i.e., on the direction of **B** with respect to the microstructure. However, when $\det \hat{\rho}_e$ is evaluated, one always gets back the asymptotic result

$$\det \hat{\rho}_e \cong R_{12}R_{23}=\rho_0^2 \nu H^2, \tag{3.12}$$

which is *independent of the direction of* **B**. Thus the H^4 behavior and the directional oscillations of the two products $\rho_{\parallel}^{(e)}\tilde{\rho}_{\perp}^{(e)}$ and $(\rho_{yz}^{(e)})^2$ will cancel each other. Evidently, Eq. (3.12) is in full agreement with the exact result of Eq. (2.17).

C. Application to the case B$\|$(011)

When $a<2b$ for the square rods—this case is covered by the discussion in Sec. III B—we simply need to put $\theta=45°$ in all the expressions obtained there. However, in that special case we find that $\rho_{yz}^{(e)}=0$, while the diagonal resistivities exhibit very different behavior at large H

$$\rho_{\parallel}^{(e)} \cong R_{23}=\frac{\nu\rho_0}{\ln 2}, \tag{3.13}$$

$$\tilde{\rho}_{\perp}^{(e)} \cong R_{12}=\rho_0 H^2 \ln 2. \tag{3.14}$$

When $a>2b$ for the square rods, a simple square network of resistors is not enough to represent this configuration. In addition to current flows between adjacent S inclusions, which can still be represented by effective resistances like R_{12} and R_{23}, there will also be uniform fields and currents in the inclusion-free, **B**-parallel M layers that now appear in between neighboring diagonal rows of inclusions. Taking all of this into account, one can again find closed form expressions for the diagonal components of $\hat{\rho}_e$ (note that, again, $\rho_{yz}^{(e)}=0$ due to the symmetry of this configuration)

$$\rho_{\parallel}^{(e)} \cong \frac{\nu\rho_0}{1-\dfrac{2b}{a}+\ln\dfrac{a}{a-b}}, \tag{3.15}$$

$$\tilde{\rho}_{\perp}^{(e)} \cong \rho_0 H^2\left(1-\frac{2b}{a}+\ln\frac{a}{a-b}\right). \tag{3.16}$$

In contrast with Eqs. (3.13) and (3.14), and with the results obtained in Sec. III B, these last results do depend on the (relative) inclusion sizes b/a.

For the case of circular cylinders, the expressions of the previous subsection are valid in the entire range $1/\sqrt{8} < R/a < 1/\sqrt{2}$, but they must be used carefully, because in the limit $\theta \to \pi/4$ one encounters vanishing denominators in some of those expressions. If one treats this case in separate fashion, one can actually obtain the results in a very explicit form, namely $\rho_{yz}^{(e)}=0$ and

$$\begin{aligned}\frac{\nu\rho_0}{\rho_{\parallel}^{(e)}} &= \frac{\tilde{\rho}_{\perp}^{(e)}}{\rho_0 H^2} \\ &= -2\arctan\left(\frac{1-\sqrt{1-\epsilon^2}}{\epsilon}\right) \\ &\quad +\frac{2(1+\epsilon)}{\sqrt{\epsilon(2+\epsilon)}}\arctan\left(\frac{\sqrt{2+\epsilon}(1-\sqrt{1-\epsilon^2})}{\epsilon^{3/2}}\right),\end{aligned} \tag{3.17}$$

where

$$\epsilon \equiv \frac{a}{\sqrt{2}R}-1, \quad \frac{1}{\sqrt{8}} < \frac{R}{a} < \frac{1}{\sqrt{2}}. \tag{3.18}$$

The last inequality means that this result is also valid when there is some overlap between nearest-neighbor cylinders, but not between next-nearest-neighbor cylinders, i.e., when $1/2 < R/a < 1/\sqrt{2}$. As was the case with the square rods, in this configuration $\rho_{\parallel}^{(e)}$ saturates when $|H| \gg 1$, and only $\tilde{\rho}_{\perp}^{(e)}$ exhibits nonsaturating H^2 behavior. Again, it is evident that all the results obtained in this section are in full agreement with Eq. (2.17).

D. Application to the case of nonoverlapping inclusions when B$\|$(001)

In this case the local current distribution is very simple, and its asymptotic form can be found from simple physical considerations: When $\langle \mathbf{E} \rangle \| \mathbf{B}$, the current is restricted to the inclusion-free parallel layers along **B**, where it is uniform—see Fig. 4(a). Therefore we easily get

$$\rho_{\parallel}^{(e)} \cong \frac{\nu\rho_0}{1-b/a} \tag{3.19}$$

for the square-rod array, and

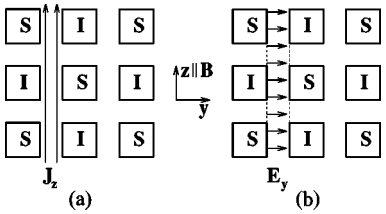

FIG. 4. Asymptotic current and field distributions for $|H|\gg 1$ in the microstructure of Fig. 1(b) when $\mathbf{B}\|z$ lies along the principal axis (001) of the square array of inclusions. (a) When $\langle\mathbf{E}\rangle\|z$, then J_z is nonnegligible and uniform only in the **B**-parallel, inclusion-free layers, while $J_y\cong 0$ everywhere. (b) When $\langle\mathbf{E}\rangle\|y\perp\mathbf{B}$, then E_y is non-negligible and uniform only in those same layers, while $E_z\cong 0$ everywhere.

$$\rho_{\|}^{(e)}\cong\frac{\nu\rho_0}{1-2R/a} \tag{3.20}$$

for the circular-cylinder array.

When $\langle\mathbf{E}\rangle\perp\mathbf{B}$, the local electric field is nonzero only in those same layers, where it is uniform and points along $\langle\mathbf{E}\rangle$—see Fig. 4(b). Again it is easily found that

$$\tilde{\rho}_{\perp}^{(e)}\cong\rho_0 H^2\left(1-\frac{b}{a}\right) \tag{3.21}$$

for the square-rod array, and

$$\tilde{\rho}_{\perp}^{(e)}\cong\rho_0 H^2\left(1-\frac{2R}{a}\right) \tag{3.22}$$

for the circular-cylinder array.

As in the case where $\mathbf{B}\|(011)$, now too $\rho_{yz}^{(e)}=0$ because of the reflection symmetry of the $\mathbf{B}\|(001)$ configuration. Also, now too the behavior of $\rho_{\|}^{(e)}$, $\tilde{\rho}_{\perp}^{(e)}$ at large H is quite different—the first one saturates while the second increases as H^2 without any saturation. All the results satisfy Eq. (2.17).

E. Results for overlapping cylindrical inclusions when $\mathbf{B}\|(001)$

When there is a finite overlap between nearest-neighbor cylinders, but not between next-nearest-neighbor cylinders, then there are no **B**-parallel layers in *M* that either connect or separate between adjacent *S* inclusions. Some reflection leads to the conclusion that, when $|H|\gg 1$, the current lines in *M* will be restricted to a narrow bundle which is parallel to *z*—see Fig. 5(a). The current distribution in this narrow region cannot be calculated exactly, even in that limit. An approximate form can be obtained by making a simple ansatz for the current profile, and including a width parameter *w* which is determined by minimizing the resulting dissipation. Assuming a triangular current profile, as shown in Fig. 5(b), we find that the dissipation is minimized when

$$w=\frac{h}{2|H|},\quad h\equiv a-\sqrt{4R^2-a^2}, \tag{3.23}$$

where *h* is the length of the current bundle and *w* is its half width, [see Figs. 5(a) and (b)] and

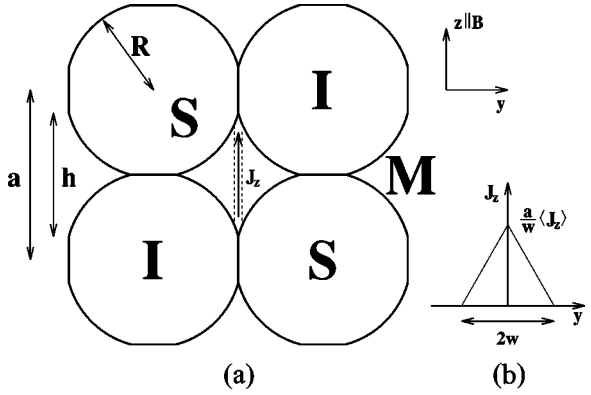

FIG. 5. Schematic drawing of a y,z section of an overlapping square array of alternating *I* and *S* cylinders, of radius *R* and nearest-neighbor center distance *a*, embedded in an *M* host. Due to the overlap, the inclusions are actually not full circular cylinders, but are truncated in such a way that adjacent *I* and *S* inclusions have flat interfaces between them. Because $\sigma_{zz}^{(M)}\gg\sigma_{yy}^{(M)}$ when $|H|\gg 1$, therefore when $\mathbf{B}\|(001)$, the current which flows through *M* between one *S* region and its nearest-neighbor *S* region is essentially restricted to a narrow bundle of flow lines along the *z* axis, of length *h*, as indicated by the dashed lines in the central *M* region. (b) Triangular profile of the current density $J_z(y)$ in that bundle, which was used as an ansatz. The value of the width parameter *w* was determined by minimizing the total dissipation.

$$\frac{\rho_{\|}^{(e)}}{\rho_0}\cong\frac{3}{2}\nu|H|,\quad\frac{\tilde{\rho}_{\perp}^{(e)}}{\rho_0}\cong\frac{2}{3}|H|. \tag{3.24}$$

Of course, $\rho_{yz}^{(e)}$ vanishes due to symmetry. The coefficients 3/2 and 2/3 which appear here are surely only approximate, since they depend on the details of the ansatz that was used for the current profile. But we think the fact that both $\rho_{\|}^{(e)}$ and $\tilde{\rho}_{\perp}^{(e)}$ exhibit nonsaturating behavior, increasing as $|H|$ when $|H|\gg 1$, is exact. We believe that the somewhat surprising conclusion, that these resistivities are *independent of the cylinder radius*, is also exact. Equation (2.17) is again satisfied.

F. Results for some nonsymmetric microstructures

Closed-form asymptotic results can also be obtained for such systems, by a straightforward application of the ideas and principles that were described in Secs. III A and III C. A few such results are presented here, for comparison with numerical computations described in Sec. IV below.

Consider a periodic square array of alternating *I*/*S* inclusions with *unequal square cross sections*, as shown in Fig. 6. For $\langle\mathbf{J}\rangle\|\mathbf{B}\|z\|(001)$ it is not difficult to calculate the uniform currents J_{z1}, J_{z2} in the two **B**-parallel layers shown in the left part of Fig. 6, where $b_S>b_I$ is assumed, i.e., the *S* rods are thicker than the *I* rods. For $\langle\mathbf{J}\rangle\|y\perp\mathbf{B}\|z\|(001)$ it is similarly easy to calculate the uniform electric field E_{y1} in the inclusion free **B**-parallel layer, as shown in the right part of that figure. Obviously, if $b_S<b_I$, then there will also be another uniform value E_{y2} of the local electric field in some other regions.

The results for macroscopic response are $\rho_{yz}^{(e)}=0$, because of the symmetry, and

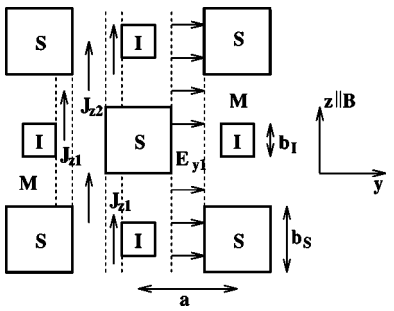

FIG. 6. Square array of alternating I and S rods, with *unequal cross sections* $b_I \times b_I$ and $b_S \times b_S$, respectively, embedded in an M host. The distance between centers of adjacent S and I rods is a. A magnetic field $\mathbf{B} \| z$ is applied along a principal axis of the array. Vertical dashed lines, which appear in the left part of the drawing, indicate where $\mathbf{J}(\mathbf{r})$ is nonnegligible in M when $\langle \mathbf{E} \rangle \| z$ and $|H| \gg 1$. Only J_z is then nonnegligible and, for $b_S > b_I$, it takes only two different values, denoted here by J_{z1}, J_{z2}. Another set of vertical dashed lines, which appear in the right part of the drawing, indicate where $\mathbf{E}(\mathbf{r})$ is nonnegligible when $\langle \mathbf{E} \rangle \| y$ and $|H| \gg 1$. Only E_y is then nonnegligible, and it takes on just one value, denoted by E_{y1}, when $b_S > b_I$. When $b_S < b_I$, then E_y can take on two different nonzero values in M, E_{y1} and E_{y2}, if $\langle \mathbf{E} \rangle \| y$, while J_z then takes on only one nonzero value if $\langle \mathbf{E} \rangle \| z$.

$$\frac{\rho_{\|}^{(e)}}{\rho_0} \cong \begin{cases} \dfrac{\nu}{1 - \dfrac{b_S}{a} + \dfrac{b_S - b_I}{a - b_I/2}}, & b_S > b_I, \\ \dfrac{\nu}{1 - b_I/a}, & b_S < b_I, \end{cases} \tag{3.25}$$

$$\frac{\tilde{\rho}_{\perp}^{(e)}}{\rho_0} \cong \begin{cases} H^2 \left(1 - \dfrac{b_S}{a} \right), & b_S > b_I, \\ H^2 \left(1 - \dfrac{b_I}{a} + \dfrac{b_I - b_S}{a - b_S/2} \right), & b_S < b_I. \end{cases} \tag{3.26}$$

The asymptotic result for the I/S constituent exchanged composite medium can now be obtained in each case by using the *other line* in Eqs. (3.25) or (3.26), and switching the roles of b_S and b_I. It is then easily seen that these results satisfy the exact relations of Eq. (2.20).

When $\mathbf{B} \| z \| (01\bar{1})$, we again find that $\rho_{yz}^{(e)} = 0$, because of the symmetry, and

$$\frac{\rho_{\|}^{(e)}}{\rho_0} \cong \begin{cases} \dfrac{\nu}{\ln \dfrac{2a - b_I - b_S}{a - b_S}}, & 1 < \dfrac{b_I + b_S}{a} < 2, \\ \dfrac{\nu}{1 - \dfrac{b_I + b_S}{a} + \ln \dfrac{a}{a - b_S}}, & \dfrac{b_I + b_S}{a} < 1, \end{cases} \tag{3.27}$$

$$\frac{\tilde{\rho}_{\perp}^{(e)}}{\rho_0} \cong \begin{cases} H^2 \ln \dfrac{2a - b_I - b_S}{a - b_I}, & 1 < \dfrac{b_I + b_S}{a} < 2, \\ H^2 \left(1 - \dfrac{b_I + b_S}{a} + \ln \dfrac{a}{a - b_I} \right), & \dfrac{b_I + b_S}{a} < 1. \end{cases} \tag{3.28}$$

The asymptotic results for the I/S constituent exchanged composite medium can be obtained by switching the roles of b_I and b_S in these equations. Again, the results satisfy the exact relations of Eq. (2.20).

IV. NUMERICAL CALCULATIONS ON PERIODIC MICROSTRUCTURES

For numerical computations on the three-constituent composites discussed in this article we used an obvious extension of the numerical approach which had been developed earlier for computing the magnetoresistivity of two-constituent periodic composites.[3,11] The local conductivity tensor $\hat{\sigma}(\mathbf{r})$ can now be written with the help of the two characteristic functions θ_I and θ_S, where $\theta_I(\mathbf{r}) = 1$ for $\mathbf{r} \in I$ while $\theta_I(\mathbf{r}) = 0$ elsewhere, and similarly $\theta_S(\mathbf{r}) = 1$ for $\mathbf{r} \in S$ while $\theta_S(\mathbf{r}) = 0$ elsewhere,

$$\hat{\sigma}(\mathbf{r}) = \hat{\sigma}_M - \delta\hat{\sigma}_I \theta_I - \delta\hat{\sigma}_S \theta_S, \tag{4.1}$$

$$\delta\hat{\sigma}_I \equiv \hat{\sigma}_M - \hat{\sigma}_I, \tag{4.2}$$

$$\delta\hat{\sigma}_S \equiv \hat{\sigma}_M - \hat{\sigma}_S. \tag{4.3}$$

Thus, whenever the combination $\delta\hat{\sigma}\theta_1(\mathbf{r})$ or $\delta\hat{\sigma}\theta_{\mathbf{g}}$ [$\theta_1(\mathbf{r})$ is the characteristic function of the inclusions in the two-constituent mixture, $\theta_{\mathbf{g}} \equiv 1/V_a \int_{V_a} \theta_1(\mathbf{r}) e^{-i\mathbf{g}\cdot\mathbf{r}} dV$ is its Fourier transform, $\mathbf{g}$ is always a reciprocal-lattice vector appropriate to the periodic microstructure] appears in those references, it now needs to be replaced by $\delta\hat{\sigma}_I \theta_I(\mathbf{r}) + \delta\hat{\sigma}_S \theta_S(\mathbf{r})$ or by its Fourier transform $\delta\hat{\sigma}_I \theta_{\mathbf{g}}^{(I)} + \delta\hat{\sigma}_S \theta_{\mathbf{g}}^{(S)}$. In this way we compute the bulk effective conductivity tensor $\hat{\sigma}_e$ of a composite with a periodic array of two types of infinitely long parallel inclusions, which are either perfectly insulating or perfectly conducting, embedded in an otherwise uniform free-electron-metal host (this means that we put $\nu = 1$ everywhere) with zero field conductivity $1/\rho_0 = 1$ and Hall-to-Ohmic resistivity ratio H. The perfectly insulating inclusions are taken to have $\hat{\sigma}_I = 0$, while the perfectly conducting inclusions are taken to have $\hat{\sigma}_S = \sigma_S \hat{I}$, where $\hat{I}$ is the unit tensor and σ_S has the large but finite value $50/\rho_0$ or $100/\rho_0$.

We first consider the I/S exchange symmetric periodic array of circular cylinders, with unit cell shown at the top of Fig. 7. In the same figure we show polar plots of all the in-plane components of $\hat{\sigma}_e$, along with the determinant $\det \hat{\sigma}_e \equiv \sigma_{\|}^{(e)} \tilde{\sigma}_{\perp}^{(e)} - (\sigma_{yz}^{(e)})^2$, plotted vs the direction of $\mathbf{B}$, as obtained from numerical computations. Also shown, in the same plots, are the predictions of the asymptotic expressions for $\hat{\sigma}_e$ and $\det \hat{\sigma}_e$, and the exact result for $\det \hat{\sigma}_e$. For the range of directions discussed in Sec. III B, the numerically calculated angular profiles are in good agreement with the results obtained by inverting the exact asymptotic expressions for the resistivity matrix $\hat{\rho}_e$, given by Eqs. (3.9)–(3.11). Along the (001)-like directions, the agreement between the computed results for $\hat{\sigma}_e$ and the asymptotic expressions of Eqs. (3.20) and (3.22) is less impressive [see the hexagonal open points in Figs. 7(a) and (b)]. The polar

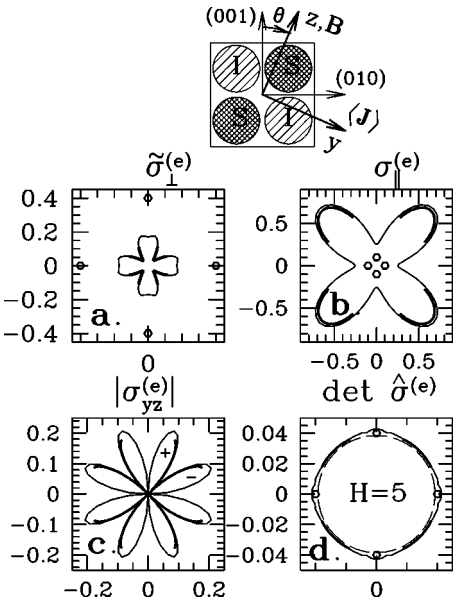

FIG. 7. Polar plots of $\tilde{\sigma}_{\perp}^{(e)}$, $\sigma_{\parallel}^{(e)}$, $\sigma_{yz}^{(e)}$, and the determinant $\det\hat{\sigma}_e=\tilde{\sigma}_{\perp}^{(e)}\sigma_{\parallel}^{(e)}-(\sigma_{yz}^{(e)})^2$, vs the direction of **B**, obtained from numerical calculations on the three constituents, I/S exchange symmetric periodic composite, with unit cell shown at the top. The infinitely long, parallel, I and S circular cylinders have radius R and distance a between nearest neighbor centers, with $R/a=0.45$, and are embedded in an otherwise uniform host with conductivity tensor $\hat{\sigma}_M$ of the form of Eq. (2.5) with $H=5$, $\rho_0=1$, $\nu=1$. Thin lines show the results of numerical calculations, boldface lines show the results obtained by inverting the 2D in-plane asymptotic resistivity tensor $\hat{\rho}_e$, given by Eqs. (3.9)–(3.11). The open hexagonal points represent results obtained in similar fashion from the asymptotic expressions (3.20) and (3.22). $\det\hat{\sigma}_e$ should always be equal to $1/[\rho_0^2\nu(1+H^2)]$, [see Eq. (2.18)] whatever the direction of **B**—this circle is shown as a dashed line in (d), while the actual values of the determinant, as obtained from the numerical results, are shown as a thin solid line. The asymptotic results for $\det\hat{\sigma}_e$ are again shown as boldface lines and hexagonal points. The ''+'' and ''−'' signs shown in (c) denote the (alternating) sign of $\sigma_{yz}^{(e)}$ in the corresponding lobe. Those signs continue to alternate from lobe to lobe. The 2D Fourier transforms $\theta_{\mathbf{g}}^{(I)}$, $\theta_{\mathbf{g}}^{(S)}$, which were used in the numerical procedure, are easily constructed from the 2D Fourier transform $\theta_{\mathbf{g}}=(2\pi R/a^2|\mathbf{g}|)J_1(|\mathbf{g}|R)$ [J_1 is a regular cylindrical Bessel function] of the characteristic function of a simple square array of identical circular inclusions (see Refs. 3 and 11 for derivations of $\theta_{\mathbf{g}}$ for this and other periodic microstructures). Throughout this article, the reciprocal-lattice vectors used in our Fourier based calculations on square arrays are given by $\mathbf{g}=(2\pi/a)(n_y,n_z)$, with the integers n_y, n_z ranging from -51 up to $+51$.

plot of $\det\hat{\sigma}_e$, which appears in Fig. 7(d), shows that the numerically computed values are in good agreement with the exact result $1/[\rho_0^2\nu(1+H^2)]$, even when $\mathbf{B}\|(001)$. We conclude that the above mentioned discrepancy is mainly due to the small value of $H=5$, which apparently is not large enough to warrant using the asymptotic expressions when **B** lies in that direction.

In Fig. 8 we show similar polar plots of the resistivity tensor components, $\tilde{\rho}_{\perp}^{(e)}$, $\rho_{\parallel}^{(e)}$, and $\rho_{yz}^{(e)}$, along with their determinant $\det\hat{\rho}_e=\rho_{\parallel}^{(e)}\tilde{\rho}_{\perp}^{(e)}-(\rho_{yz}^{(e)})^2$, vs the direction of **B**. The microstructure and physical parameters are the same as

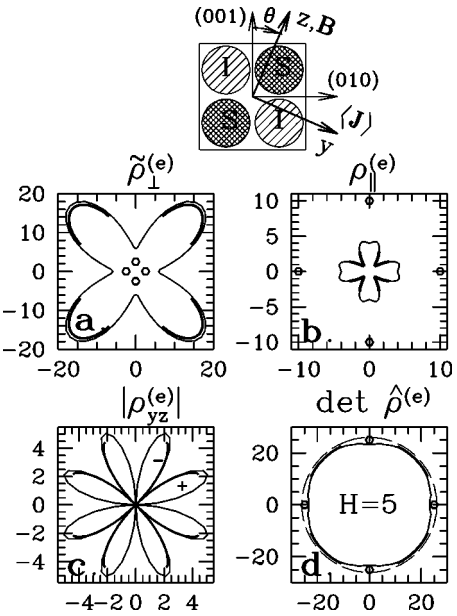

FIG. 8. Polar plots of the resistivity tensor components $\tilde{\rho}_{\perp}^{(e)}$, $\rho_{\parallel}^{(e)}$, $\rho_{yz}^{(e)}$, and the determinant $\det\hat{\rho}_e=\rho_{\parallel}^{(e)}\tilde{\rho}_{\perp}^{(e)}-(\rho_{yz}^{(e)})^2$, vs the direction of **B** for the *same microstructure* that was the subject of Fig. 7. The physical parameters used are also identical, as are the particular notations, namely thin line, boldface line, dashed line, hexagonal points, $+/-$ signs. $\det\hat{\rho}_e$ should always be equal to $\rho_0^2\nu(1+H^2)$, whatever the direction of **B**—that circle is shown in (d) as a dashed line.

in Fig. 7. The level of agreement between numerically computed and asymptotic results for the components of $\hat{\rho}_e$, and between both of those results and the exact results for $\det\hat{\rho}_e$, is similar to that found in Fig. 7. We note that Eq. (2.19) predicts that the angular profiles of $\rho_{\parallel}^{(e)}$, $\tilde{\rho}_{\perp}^{(e)}$, and $\rho_{yz}^{(e)}$ should be the same as those of $\tilde{\sigma}_{\perp}^{(e)}$, $\sigma_{\parallel}^{(e)}$, and $-\sigma_{yz}^{(e)}$, respectively, up to the factor $\rho_0^2\nu(1+H^2)$. This is satisfied by the numerical computations, as is clearly evident when we compare Figs. 7 and 8.

Figure 9 shows plots similar to those of Fig. 8, but for the case of a square array of square cross section, $(b\times b)$, alternating I and S rods instead of cylinders. In order to verify our numerical scheme, we also calculated angular profiles for the same microstructure using a different definition of the unit cell. Those results, as well as the new unit cell, are shown in Fig. 10. The microstructure has now been rotated by 45°, therefore the angular profiles of $\tilde{\rho}_{\perp}^{(e)}$, $\rho_{\parallel}^{(e)}$, and $\rho_{yz}^{(e)}$ are also rotated by the same angle, as compared to those of Fig. 9.

In Fig. 11 we show results for a square array of alternating I and S cylindrical inclusions which are now large enough so that nearest-neighbor cylinders exhibit some overlap. For this reason, neighboring I and S inclusions are separated by a flat interface, as shown in Fig. 5(a) and at the top of Fig. 11. Equations (3.9)–(3.11) are now applicable to all directions of **B**, with the exception of the (001)-like directions, where the asymptotic behavior is given by Eq. (3.24). The level of agreement between numerical computations, asymptotic expressions, and exact results is similar to what was found in the previous examples.

In Fig. 12 we show results for a square array of alternat-

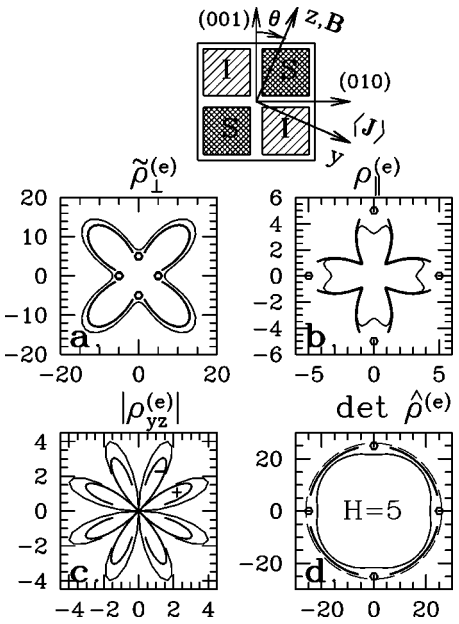

FIG. 9. Similar to Fig. 8, but for a composite where the inclusions have the shape of square cross-section ($b\times b$) rods with distance a between nearest-neighbor I and S rod centers, where $b/a=0.8$—the unit cell is shown at the top. The same physical parameters and notations are used as in Figs. 7 and 8. The 2D Fourier transforms $\theta_{\mathbf{g}}^{(I)}$, $\theta_{\mathbf{g}}^{(S)}$ are easily constructed from the 2D Fourier transform $\theta_{\mathbf{g}}=[\sin(g_y b/2)/g_y b/2][\sin(g_z b/2)/g_z b/2]$ of the characteristic function of a simple square array of identical rod-shaped inclusions.

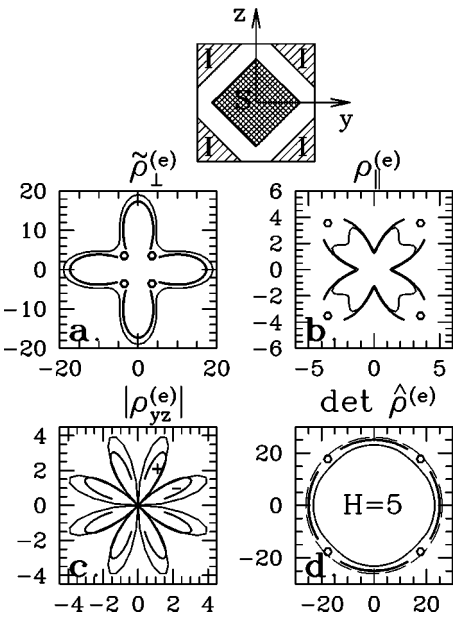

FIG. 10. Polar plots of the resistivity tensor components $\tilde{\rho}_\perp^{(e)}$, $\rho_\parallel^{(e)}$, $\rho_{yz}^{(e)}$, and the determinant $\det\hat{\rho}_e=\rho_\parallel^{(e)}\tilde{\rho}_\perp^{(e)}-(\rho_{yz}^{(e)})^2$, vs the direction of **B** for the *same microstructure* that was the subject of Fig. 9, but the calculations are performed using an alternative unit cell, shown at the top. The resulting microstructure, though identical to the one of Fig. 9, is rotated by 45°. Consequently, the polar plots should be the same as those of Fig. 9 but also rotated by that same angle.

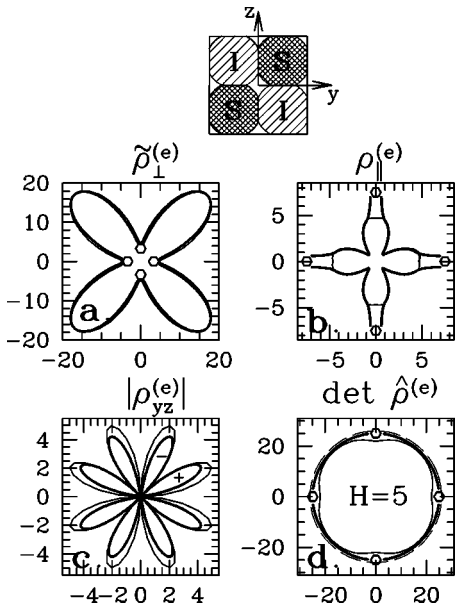

FIG. 11. Polar plots of the resistivity tensor components $\tilde{\rho}_\perp^{(e)}$, $\rho_\parallel^{(e)}$, $\rho_{yz}^{(e)}$, and the determinant $\det\hat{\rho}_e=\rho_\parallel^{(e)}\tilde{\rho}_\perp^{(e)}-(\rho_{yz}^{(e)})^2$, vs the direction of **B** for a symmetric, periodic square array of alternating I/S circular cylinders with *partial overlap* of nearest-neighbor I and S cylinders—the unit cell is shown at the top. The cylinder radius R and nearest-neighbor center distance a satisfy $R/a=0.56$, while $H=5$. Notations are the same as in Figs. 7 and 8, but note that the small hexagons now denote asymptotic results which are only approximate—see Eqs. (3.24) and the discussion in Sec. III E. The 2D Fourier transforms $\theta_{\mathbf{g}}^{(I)}$, $\theta_{\mathbf{g}}^{(S)}$ are now constructed from the 2D Fourier transform of the characteristic function of a simple square array of identical overlapping or truncated circular inclusions: $\theta_{\mathbf{g}}=(2\pi R/a^2|\mathbf{g}|)J_1(|\mathbf{g}|R)-(4/a^2 g_y g_z)[I(g_y,g_z)+I(g_z,g_y)]$, where $I(u,v)\equiv u\int_0^{\sqrt{R^2-a^2/4}}dx\,\cos(ux)\sin(v\sqrt{R^2-x^2})-\sin(ua/2)\sin(v\sqrt{R^2-a^2/4})$.

ing square cross-section rods which is not symmetric under the exchange of I and S inclusions, because the two types of rods have different thicknesses. In this case $\det\hat{\rho}_e$ is no longer independent of the direction of **B**, however, there are other combinations of the components of $\hat{\rho}_e$ and $\hat{\rho}_{ex}$ which have that property—see Eq. (2.20). Some of those are plotted in Fig. 12, along with the angular profiles of the different components of $\hat{\rho}_e$ and $\hat{\rho}_{ex}$.

The deviations of the numerically computed values of those combinations from the precisely predicted circular plots, as well as the deviations of the numerically computed values of $\det\hat{\sigma}_e$ and $\det\hat{\rho}_e$ from the precisely predicted circular plots in Figs. 7–11, can be ascribed to imperfect convergence of the numerical computations, and to the fact that the ''perfectly conducting inclusions'' were only 50 or 100 times more conducting than the normal conductor host: When the number of harmonics retained in the Fourier-based numerical scheme is increased, those deviations decrease, but they do not tend to 0 (see Refs. 3 and 11 for a detailed description of the numerical scheme). Those deviations provide a good measure for the accuracy of the numerical computations, and also for the penalty which results from using a large but finite value, instead of ∞, for σ_S.

In contrast with the above described small discrepancies

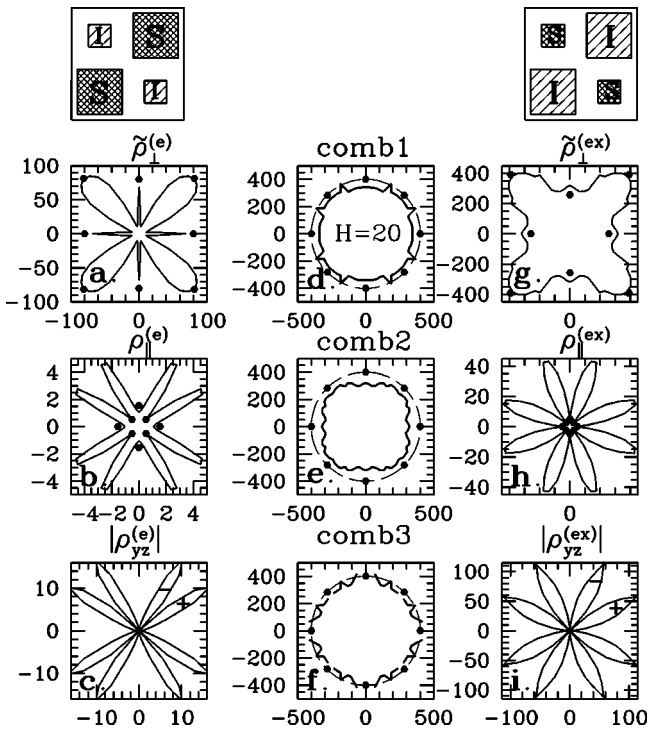

FIG. 12. (a)–(c): Polar plots of $\tilde{\rho}_{\perp}^{(e)}$, $\rho_{\parallel}^{(e)}$, $\rho_{yz}^{(e)}$ for a *nonsymmetric* periodic square array of alternating I/S square cross-section rods of widths b_I and b_S, respectively, and distance a between centers of nearest-neighbor rods. Those sizes are given by $b_I/a=0.4<b_S/a=0.8$—the unit cell is shown at the top left. Solid lines show results of numerical computations for $H=20$, with the other physical parameters the same as in Fig. 7, while the black circles show results of the asymptotic expressions Eqs. (3.25)–(3.28). (g)–(i): The same as (a)–(c) but for the components of $\hat{\rho}_{ex}$, the bulk effective resistivity tensor of the I/S exchanged microstructure, with unit cell shown at the top right. (d), (e), (f): Polar plots vs the direction of **B** of three combinations of components of $\hat{\rho}_e$ and $\hat{\rho}_{ex}$, which are predicted to be independent of that direction: comb1 $=\tilde{\rho}_{\perp}^{(ex)}\det\hat{\rho}_e/\tilde{\rho}_{\perp}^{(e)}$, comb2$=\rho_{\parallel}^{(ex)}\det\hat{\rho}_e/\rho_{\parallel}^{(e)}$, and comb3 $=\rho_{yz}^{(ex)}\det\hat{\rho}_e/\rho_{yz}^{(e)}$. All three combinations should be equal to $\rho_0^2\nu(1+H^2)$. That prediction appears as a dashed line circle in these plots, along with a solid line which represents the numerical computations and black points which represent the asymptotic results.

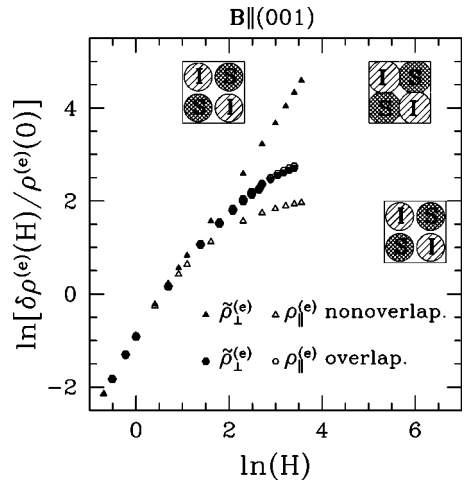

FIG. 13. Log-log plots of $\delta\tilde{\rho}_{\perp}^{(e)}/\rho^{(e)}(0)$ and $\delta\rho_{\parallel}^{(e)}/\rho^{(e)}(0)$ [where $\delta\rho_{\parallel}^{(e)}\equiv\rho_{\parallel}^{(e)}(H)-\rho_{\parallel}^{(e)}(H=0)$, etc.] vs H, obtained from numerical calculations on an I/S exchange symmetric square array of alternating I/S circular-cylinder inclusions when $\mathbf{B}\|(001)$. In one case the radius R and nearest-neighbor center separation a satisfy $R=0.45a$, so that there are no overlaps, while in the other case they satisfy $R=0.56a$, so that nearest-neighbor cylinders partially overlap—the unit cells are shown in proximity to the relevant points. When there are no overlaps, the results agree with the prediction that $\rho_{\parallel}^{(e)}$ saturates but $\tilde{\rho}_{\perp}^{(e)}\sim H^2$ when $|H|\gg 1$ [see Eqs. (3.20) and (3.22)]. In the other case, where, due to the partial overlap, all cylinders are truncated and nearest-neighbor I and S (truncated) cylinders have a flat interface, the results agree with the prediction that both components $\tilde{\rho}_{\perp}^{(e)}$ and $\rho_{\parallel}^{(e)}$ increase as $|H|$ when $|H|\gg 1$ [see Eq. (3.24)]. The physical parameters, with the exception of H, are the same as in Fig. 7. Note that both $\delta\rho_{\parallel}^{(e)}$ and $\delta\tilde{\rho}_{\perp}^{(e)}$ increase as H^2 for both microstructures when $|H|\ll 1$. Note also that $\rho_e(H=0)=\rho_0$ according to Eq. (2.22) and its sequel.

in the values of $\det\hat{\sigma}_e$ and $\det\hat{\rho}_e$, the differences between the numerically computed values of the *components* of $\hat{\sigma}_e$, $\hat{\rho}_e$ and the values predicted by some of the exact asymptotic expressions usually have another significance: The rate at which $\hat{\rho}_e$ tends to its $|H|\gg 1$ asymptotic behavior is sometimes nonuniform. Figures 7–11 show that as the direction of **B** approaches one of the (001)-like directions, i.e., when $\theta\to 0$, those differences sometimes increase drastically for the value $H=5$ that was assumed in those calculations. Other computations, done at greater values of H, show that those differences decrease with increasing $|H|$. For example, Fig. 12 shows results for $H=20$: Those numerical computations of $\hat{\rho}_e$ agree well with the asymptotic expressions even when $\mathbf{B}\|(001)$. In some cases, as when neighboring I and S cylinders partially overlap (see Fig. 11), one finds that for any finite value of H, no matter how large, the actual results deviate from the asymptotic predictions when θ is sufficiently small.

In Figs. 13 and 14 we plot the H dependence of various components of $\hat{\rho}_e$ under different conditions. In Fig. 13 we show log-log plots of $\delta\rho_{\parallel}^{(e)}/\rho^{(e)}(0)$ and $\delta\tilde{\rho}_{\perp}^{(e)}/\rho^{(e)}(0)$ $[\delta\rho^{(e)}(H)\equiv\rho^{(e)}(H)-\rho^{(e)}(0)]$ vs H when **B** lies along one of the (001)-like directions. Two types of alternating I/S square arrays are considered: Circular-cylinder inclusions with and without overlap of nearest neighbor I and S inclusions. Completely different behavior is found in those two cases for $\tilde{\rho}_{\perp}^{(e)}$ and $\rho_{\parallel}^{(e)}$: In the case of nonoverlapping inclusions the in-plane transverse component $\tilde{\rho}_{\perp}^{(e)}$ increases as H^2 when $|H|\gg 1$, in accordance with Eq. (3.22), while the longitudinal component $\rho_{\parallel}^{(e)}$ saturates, in accordance with Eq. (3.20). However, when neighboring I and S inclusions do overlap, both components $\tilde{\rho}_{\perp}^{(e)}$ and $\rho_{\parallel}^{(e)}$ increase as $|H|$ for $|H|\gg 1$, in accordance with Eq. (3.24). Note that $\rho_{yz}^{(e)}$ vanishes for **B** in those directions. Note also that, according to Eq. (2.22) and its sequel, we should expect to get $\rho_e(H=0)=\rho_0$. However, because the conductivity σ_S of the S inclusions was taken to be only 50 or 100 times greater than $1/\rho_0$, instead of ∞, $\rho_e(H=0)$ should be somewhat greater than ρ_0. In practice, this scenario is observed only if σ_S is not so large, or if the total number of **g** vectors retained in

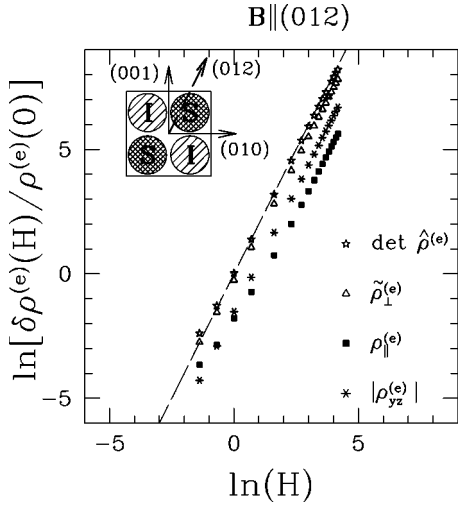

FIG. 14. Log-log plots of $\delta\tilde{\rho}_{\perp}^{(e)}/\rho^{(e)}(0)$, $\delta\rho_{\parallel}^{(e)}/\rho^{(e)}(0)$, $\rho_{yz}^{(e)}$, and $\delta\det\hat{\rho}_e/\det\hat{\rho}_e(0)$ [where $\delta\det\hat{\rho}_e\equiv\det\hat{\rho}_e(H)-\det\hat{\rho}_e(0)$ and $\det\hat{\rho}_e=\tilde{\rho}_{\perp}^{(e)}\rho_{\parallel}^{(e)}-(\rho_{yz}^{(e)})^2$], vs H, obtained from numerical calculations on the composite with the same microstructure and physical parameters as in Fig. 7, except for H, when $\mathbf{B}\|(012)$. All components of $\hat{\rho}_e$, as well as $\det\hat{\rho}_e$, are now predicted to increase as H^2 for large H, as shown by the slope of the straight dashed line, and this is verified by these calculations. The behavior exhibited by $\delta\det\hat{\rho}_e$ or $\det\hat{\rho}_e$ when $|H|\gg 1$ is highly nontrivial, since it requires cancellation of the H^4 behavior of the separate contributions $\tilde{\rho}_{\perp}^{(e)}\rho_{\parallel}^{(e)}$ and $(\rho_{yz}^{(e)})^2$—see the discussion following Eq. (3.12). Note that all the quantities plotted here increase as H^2 not only when $|H|\gg 1$, but also when $|H|\ll 1$.

the Fourier-based computations is increased to an even greater number than indicated in the caption of Fig. 7. Thus it appears that the convergence of those computations with increasing total number of **g** vectors is nonuniform with respect to σ_S: That convergence becomes much slower when $\sigma_S\to\infty$.

When **B** lies along a direction which lacks reflection symmetry, such as the (012) lattice axis in these microstructures, then $\rho_{yz}^{(e)}$ no longer vanishes and the situation is quite different. In Fig. 14 we show log-log plots of $\delta\tilde{\rho}_{\perp}^{(e)}/\rho^{(e)}(0)$, $\delta\rho_{\parallel}^{(e)}/\rho^{(e)}(0)$, $\rho_{yz}^{(e)}$, and $\delta\det\rho_e$ vs H for the case of nonoverlapping cylindrical inclusions when $\mathbf{B}\|(012)$. In this case $\rho_{\parallel}^{(e)}$ no longer saturates at large H. For such directions all components of $\hat{\rho}_e$ increase as H^2 when $|H|\gg 1$. Consequently the product $\tilde{\rho}_{\perp}^{(e)}\rho_{\parallel}^{(e)}$, as well as the squared off-diagonal resistivity component $(\rho_{yz}^{(e)})^2$, increase as H^4. Nevertheless, $\det\hat{\rho}_e$ only increases as H^2: The leading H^4 behavior of those two products cancels, leaving only an H^2 behavior for the determinant, as explained right after Eq. (3.12).

Although this article has mostly focused on the behavior of $\hat{\rho}_e$ in the strong-field regime, where $|H|>1$, it is worth noting that all the components of $\delta\hat{\rho}_e$ increase as H^2 in the weak-field regime, where $|H|\ll 1$. This is clearly evident from the numerical results plotted in Figs. 13 and 14. The weak-field regime will be discussed in detail in a future publication.

V. SUMMARY AND DISCUSSION

General principles were developed for asymptotic analysis of macroscopic magnetotransport in three-constituent, $M/I/S$ composites with a columnar microstructure, and with a magnetic field perpendicular to the columnar axis. We showed that the mathematical treatment can be reduced to that of a strictly 2D microstructure, where the M constituent has a very anisotropic conductivity tensor but no Hall effect (i.e., no antisymmetric components). The crucial role of the ''**B**-parallel connecting layers'' and the ''**B**-parallel separating layers'' between neighboring S inclusions was established. It was then exploited in order to construct a resistor network model for representing the strong-field macroscopic magnetotransport behavior of periodic $M/I/S$ microstructures. We believe that the same approach will also be useful in the study of strong-field magnetotransport in random columnar $M/I/S$ microstructures.

Those general principles were used in order to study strong-field magnetotransport in some periodic $M/I/S$ columnar microstructures. In many cases we were able to get exact closed form expressions for the asymptotic macroscopic conductivity tensor $\hat{\sigma}_e$. Numerical computations of $\hat{\sigma}_e$, performed for large but finite values of H, were in good agreement with those expressions. The components of $\hat{\sigma}_e$ and $\hat{\rho}_e\equiv 1/\hat{\sigma}_e$ were found to exhibit strong oscillations as functions of the direction of **B**. Those are qualitatively similar to the oscillations found in two-constituent M/I and M/S columnar composites with a periodic microstructure. However, there appear some interesting quantitative differences: Note, in particular, the very sharp features in the angular plot of $\tilde{\rho}_{\perp}^{(e)}$ vs the direction of **B**, which appear when $\mathbf{B}\|(001)$, in the case of an asymmetric square array of square cross-section rods—see Fig. 12(a). We also note that in the case where the nearest-neighbor S and I cylinders of an alternating square array overlap partially, so that the M constituent (i.e., the host) fails to percolate in the plane perpendicular to the columnar axis, the local current distribution becomes quite singular when $|H|\gg 1$. This drastically alters the asymptotic behavior of both $\rho_{\parallel}^{(e)}$ and $\tilde{\rho}_{\perp}^{(e)}$ when $\mathbf{B}\|(001)$—see Fig. 13: Whereas $\rho_{\parallel}^{(e)}\propto H^0$ and $\tilde{\rho}_{\perp}^{(e)}\propto H^2$ when there is no overlap, both $\rho_{\parallel}^{(e)}$ and $\tilde{\rho}_{\perp}^{(e)}$ increase as $|H|$ when there is partial overlap between those cylinders. This is due to concentration of the local current density in the M constituent into a narrow bundle, of width $\propto 1/|H|$, along **B**. This behavior should make the directional oscillations of both $\rho_{\parallel}^{(e)}$ and $\tilde{\rho}_{\perp}^{(e)}$ even more violent when H is very large.

It would be interesting to try and test some of these detailed predictions in a real composite medium. Also, the strong oscillations of both $\rho_{\parallel}^{(e)}$ and $\tilde{\rho}_{\perp}^{(e)}$ with changing direction of **B** are not only interesting in themselves, but may perhaps have some useful applications in the development of magnetic field sensors that are very sensitive to that direction.

In order to make composite samples where these phenomena might be observed, it would be necessary to use constituents M, I, S with transverse Ohmic resistivities ρ_M, ρ_I, ρ_S, and Hall-to-transverse-Ohmic-resistivity ratio H of the M constituent, that satisfy the following chain of inequalities:

$$\rho_S \ll \rho_M \ll H^2 \rho_M \ll \rho_I . \tag{5.1}$$

This can be achieved by using a doped semiconductor film as the M host, with perpendicular holes etched into it as the I inclusions, as was done in Ref. 4, and with perpendicular, high conductivity metallic inclusions playing the role of the S constituent. If Si-doped GaAs is used as the M host, with a negative charge carrier density of 1.6×10^{18} cm^{-3} and a mobility $\mu = 2500$ cm^2/V s at a temperature of 90 K, as in the experiment described in Ref. 4, then a magnetic field of 40 T would result in $H=-10$. Such a material would have an Ohmic resistivity of $1.6\times 10^{-3}\,\Omega$ cm, about 1000 times greater than that of Copper. Thus, using Copper for the S inclusions and etched holes for the I inclusions, there should be no difficulty in satisfying all the above inequalities.

Although all the calculations described in this article assumed that the system was infinite in size, previous work on two-constituent M/I columnar composites examined in some detail the effects of finite film thickness.[15] It was argued there that, whenever the film thickness l and the heterogeneity length scale a satisfy $a/l \ll \max(1,|H|)$, the infinite thickness limit should be a good approximation. From numerical computations on finite thickness films of that type it was found that, when $l \approx a$ and $H=3$, the magnitude of the bulk effective resistivities was about 2/3 of their infinite thickness values.[15]

We showed that, when $|H| \gg 1$, one could often represent the electrical transport between two S inclusions by a single effective Ohmic resistance. For a periodic array of inclusions, this meant that the macroscopic system response could be mimicked by that of an ordered resistor network, if the inclusions are large enough and if the angle θ between **B** and the closest principal axis of the array is not too small. This kind of representation, by a resistor network, may be even more useful in the study of properties of disordered $M/I/S$ columnar composites, where we would be able to numerically simulate an ensemble of appropriately constructed random resistor networks. Such a study is currently in progress.

We used the classical duality transformation of 2D electrical conductivity to derive exact relations between the bulk effective resistivities of an $M/I/S$ columnar composite with an arbitrary microstructure and those of the ''I/S constituent exchanged composite.'' Those relations can be quite useful in providing a measure for the accuracy of numerical computations of those resistivities.

ACKNOWLEDGMENTS

This research was supported in part by grants from the US-Israel Binational Science Foundation, the Israel Science Foundation, the Ministry of Absorption of the State of Israel, and NSF Grant No. DMR 97-31511.

*Present address: Minerva Center and Department of Physics, Bar Ilan University, Ramat Gan 52900, Israel.

[1] P. M. Levy, Solid State Phys. **47**, 367 (1994).
[2] M. A. M. Gijs and G. E. W. Bauer, Adv. Phys. **40**, 286 (1997).
[3] D. J. Bergman and Y. M. Strelniker, Phys. Rev. B **49**, 16 256 (1994).
[4] M. Tornow, D. Weiss, K. v. Klitzing, K. Eberl, D. J. Bergman, and Y. M. Strelniker, Phys. Rev. Lett. **77**, 147 (1996).
[5] D. J. Bergman and Y. M. Strelniker, Phys. Rev. Lett. **80**, 3356 (1998).
[6] D. J. Bergman and Y. M. Strelniker, Phys. Rev. B **59**, 2180 (1999).
[7] Y. M. Strelniker and D. J. Bergman, Phys. Rev. B **61**, 6288 (2000).
[8] D. J. Bergman and Y. M. Strelniker, Phys. Rev. B **60**, 13 016 (1999).
[9] D. J. Bergman, this issue, Phys. Rev. B **62**, 13 820 (2000).
[10] D. J. Bergman and Y. M. Strelniker, Europhys. Lett. **45**, 605 (1999).
[11] Y. M. Strelniker and D. J. Bergman, Phys. Rev. B **50**, 14 001 (1994).
[12] D. J. Bergman and Y. M. Strelniker, Superlattices Microstruct. **23**, 547 (1998).
[13] A. M. Dykhne, Zh. Éksp. Teor. Fiz. **59**, 110 (1970) [Sov. Phys. JETP **32**, 63 (1971)].
[14] K. S. Mendelson, J. Appl. Phys. **46**, 4740 (1975).
[15] D. J. Bergman and Y. M. Strelniker, Phys. Rev. B **51**, 13 845 (1995).